THE UNIVERSITY of EDINBURGH

Edinburgh Research Explorer

Evolution of Thin-Liquid Films Surrounding Bubbles in Microfluidics and Their Impact on the Pressure Drop and Fluid Movement

OPEN ACCESS

Evolution of thin liquid films surrounding bubbles in microfluidics and its impact on the pressure drop and fluid movement

Cong Chao[1], Xiaoqiang Jin[1], Xianfeng Fan*

School of Engineering, The University of Edinburgh, The King's Buildings, Robert Stevenson Road, Edinburgh, EH9 3JL, UK

Corresponding author* Email: x.fan@ed.ac.uk

Abstract

Evolution of thin liquid film in a microchannel is one of the most critical and intricate phenomena to understand two-phase movement, evaporation, micro mixing, heat transfer, chemical synthesis, biological processes, and efficient energy devices. In this paper, we demonstrate experimentally the effect of liquid film on the removal of initially dry and lodged bubble in laser-etched PMMA microfluidic networks, and discuss the evolution of the liquid film in accordance with the bubble superficial velocity and the effect of liquid properties and branch angle on the evolution of the liquid film and the pressure drop. During the removal of a dry bubble, four stages have been observed in bubble velocity profiles and they directly relate to the evolution of liquid film. The correlation of maximum bubble velocity has been derived as a function of bubble length, fluid viscosity, surface tension, geometry of cross-sectional area and dimension of microchannel, which agrees with the experimental results. The bubble moving distance required for the full deposition of a continuous and stable thin liquid film is affected by the liquid viscosity and network branch angle. The liquid with a

---

[1]. These authors contributed equally to this work.

higher viscosity will increase the pressure drop for removing dry bubbles from microfluidic networks, while this effect will be hampered by increasing the microfluidic network complexity. The deposition of thin liquid film surrounding bubbles significantly decreases the pressure drop required to remove bubbles from microfluidics. Compared with DI water, the glycerol solution is prone to act as the lubricating liquid due to its strong H-bond interaction with channel wall and the reduction in interfacial energy of gas-water interface.

Introduction

Multiphase flow is always encountered in biological and engineering fluid transport processes[1-4]. When a gas-liquid or liquid-liquid interface transports through a microchannel of the porous medium, a thin liquid film is usually formed between liquid or gas phase and the channel wall. This thin liquid film plays a considerable role in governing two- or three-phase interface movement, chemical reaction pathways, catalytic performance and the heat and mass transfer rate in a wide range of systems[5-7]. The thin liquid film has been intensively investigated in terms of the measurement of steady film thickness[3, 8-9], derivation of theoretical correlation with Ca and Re number[10], and film rupture (dewetting) in microchannels[11-14]. However, the evolution of a thin liquid film around a 'dry' bubble, and the effect of thin liquid film on the removal of a dry bubble from microfluidics with micro-patterned surface remains unclear. A dry bubble means that there is no thin liquid film between the gas phase and the channel wall.

Many investigations on the thickness of liquid films have been conducted both experimentally and numerically, especially for two-phase (liquid-liquid or gas-liquid)

slug and annular flow[3, 8, 10, 15], as the thickness of liquid film significantly affects the mass and heat transport rate in microfluidics for biological and chemical engineering applications. Since 1961, the theoretical lubricating equation has been proposed by Taylor[16] and Bretherton[17] to predict the thickness of liquid film surrounding a moving elongated bubble in circular microchannels. For a conformal liquid film which is uniform without any gradient in film curvature on flat surfaces, cylinders and spheres, its thickness scales with $Ca^{2/3}$, and pressure drop over the bubble is dominated by Re number and Ca number. With the development of visualization techniques, such as shadowgraph technique, laser-induced fluorescence (LF), and laser focus displacement meter, measurement of liquid films thickness becomes more accurate[8-9, 18]. Empirical correlations for the film thickness have been therefore proposed to correct the lubricating equation for the fluids with a larger range of Ca number, or inertial force involved[8, 10, 19].

However, more attention is required to investigate the metastable state of the liquid film in terms of wall features and dynamics of two-phase interface. The wall features of microchannels significantly affect the stability of thin liquid films, its thickness, and pressure loss over the interface. The effect of surface roughness, low-wettability of surface and localized curvature gradients in liquid film thickness may result in the hydrodynamic instability of liquid film. With any small perturbation, the rupture of non-conformal thin films occurs[12, 14, 20], and it will lead to the direct contact between the interface and channel surface, which hinders the migration of the gas-liquid or liquid-liquid interface[13]. On the other hand, dynamics of dry bubbles or droplets will affect the evolution of thin liquid film deposition. Investigation on the mutual effect between dynamics of dry bubbles/droplets and evolution of thin liquid film is necessary especially for non-ideal, non-flat surfaces such as in oil reservoir, soil, microfluidic

networks (e.g. technical-treated PMMA and PDMS[21-22]), channels with irregular cross sections[14].

In microfluidic networks, bubble lodgment is always undesirable as it affects the mixing and transport efficiency and hinders the system performance. For example, bubble accumulation on the surface of PDMS-based microfluidic channel is very common in cell culturing, while bubble blockage influences the transport of nutrients and metabolites, which is vital to the cell culture[23-25]. What kind of role of the liquid film plays in the initiation of bubble dislodgment remains unclear. Kreutzer et al[14] observed that the liquid film does not exist for moving bubbles with Ca number below 2.5×10^{-5}. It suggests that the liquid film may not spontaneously deposit between these lodged bubbles and non-circular microchannel wall, especially for the non-ideal surfaces. Jose and Cubaud found that the liquid film closely affects the shape of silicon oil droplets with $10^{-4} < Ca < 10$ in square PDMS microchannels[1,26]. Mohammadi and Sharp demonstrated that the non-existence of the thin liquid film attributes to the pinning force which is the threshold to remove dry bubbles with long length ($L/D \geq 1$, L is the bubble length, D is the bubble diameter) in surface-treated glass microchannels[27]. Most researchers mainly focus on the dynamics of lubricated bubbles in which the liquid film has already been fully deposited[17, 22, 28-30], and the dewetting of the thin liquid film around moving bubbles in microfluidics[13-14]. However, understanding of how the liquid film affects the initiation of the movement of a lodged bubble is important for bubble removal from the microfluidic network.

With the increasing application of partially wetting surfaces, bubbles that are lodged and are not fully lubricated by thin and steady liquid film, should be taken into account. The dynamics of dry bubbles require further investigations in terms of the evolution of liquid film deposition between the bubble and channel wall, as the evolution of liquid

film significantly determines the resistance applied on the bubble during the removal of lodged bubble from a microchannel. Our group have investigated the pressure required for removing dry bubbles (1<L/D<5) from microfluidic networks with multiple bifurcations and highly-interconnected micro-branches[31-32]. In this study, investigations focus on the evolution of liquid film deposition between the dry bubble and non-ideal surface, and its relationship with the bubble dynamics during the bubble removal. A theoretical correlation of maximum bubble velocity within the bubble removal process has been derived as a function of bubble length, fluid viscosity, surface tension, geometry of cross-sectional area and dimension of microchannel. Experiments were designed by using networks with different branch angles and working liquids with different weight percentages of glycerol. The impact of liquid film properties (the lubricating ability, wetting/dewetting speed) and network branch angle on the dynamics of bubble removal and the pressure drop have been highlighted. The investigation on the spatiotemporal evolution of thin liquid film deposition will promote the determination and prediction of the mass and heat transport rate for two- or multi-phase flows. As some literature utilizes glycerol to prepare the blood-mimicking fluid with the dynamic viscosity ranging between 4 to 5 cP[33-35], the experimental results obtained in this study are also expected to further facilitate the understanding of fluids transport in microfluidics *in vitro*, such as the air embolotherapy in blood vessels.
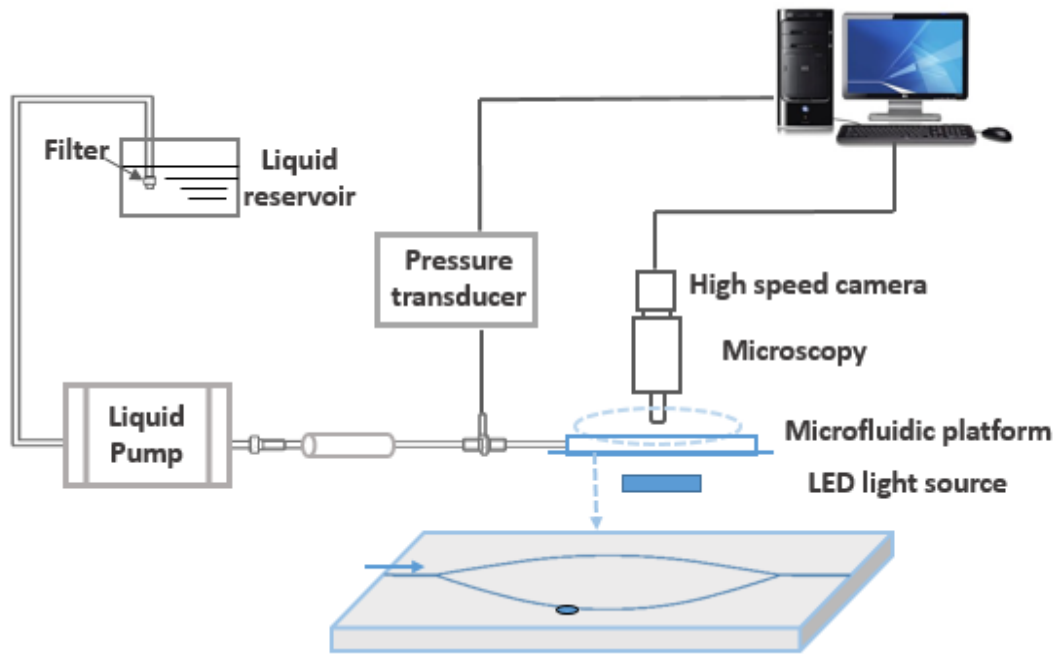
Methods and materials

Experimental setup and experimental procedures

Fig. 1(a) shows the schematic diagram of the experimental setup. Microfluidic Networks 1-4, as shown in Fig. 1(b) are composed of two branches with smoothly
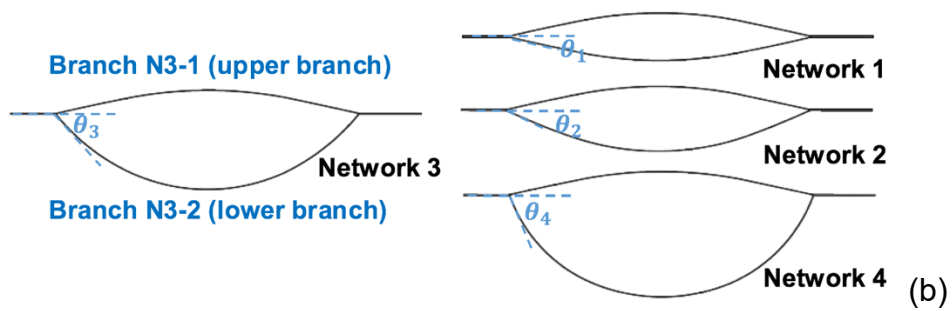
changed flow path, and the inner width and height of two branches are both approximately 350 µm. The angle of the lower branch ($\theta_1 \sim \theta_4$) is defined as the angle between the parent's medial axes and daughter's medial axes measured in the plane, which varies from 12° to 66°, as shown in Fig. 1(b). Networks 1-4 were manufactured through soft lithography technique (Epilog laser fusion M2) in a PMMA sheet (2 mm, Acrylic Cast, AMARI). To ensure the surface roughness and surface condition (cleanness and wearing) of the microfluidic networks are identical, the laser power and speed of required to etch the PMMA surface was controlled to be the same. The surface was then washed by using 70 wt. % 2-proponal solution, rinsed thoroughly with DI water. The periodic pattern on the laser-treated network surface was characterized by the surface roughness, as shown in Fig. 1 (c). The brightfield microscope image was acquired by using a Leica DMIRB inverted microscope equipped with a 20x/0.4 N.A objective lens (NPLAN, Leica) and an Andor Zyla 5.5 camera. Micromanager 2.0 software was used to capture images and control the microscope stage for mapping large areas of the laser-etched sample. Tapping mode AFM images were acquired using a Veeco Explorer atomic force microscope (AFM) with RTESPA-300 AFM probes (Bruker) at a resonance frequency of 300 kHz.

The liquid pump with a resolution of 0.0001 ml/min (LX-20 AD, Shimadzu) was employed to drive the liquid into the microfluidic network in a controlled flowrate of 0.1 ml/min. DI water and aqueous glycerol solutions with different mass concentration were used as the working liquids, and physical properties were listed in Table 1. One air bubble was slowly introduced to one branch of the network which was initially filled with liquid, and the bubble tends to be lodged and 'attached' on the surface of the branch at a low fluid velocity. Increasing the driving pressure gradually, the bubble started to be deformed, and then moved once the driving pressure is adequate. The

pressure drop was measured through the pressure transducer (DPI 280, Druck) with a resolution of 0.01 mbar, and recorded with Labview.
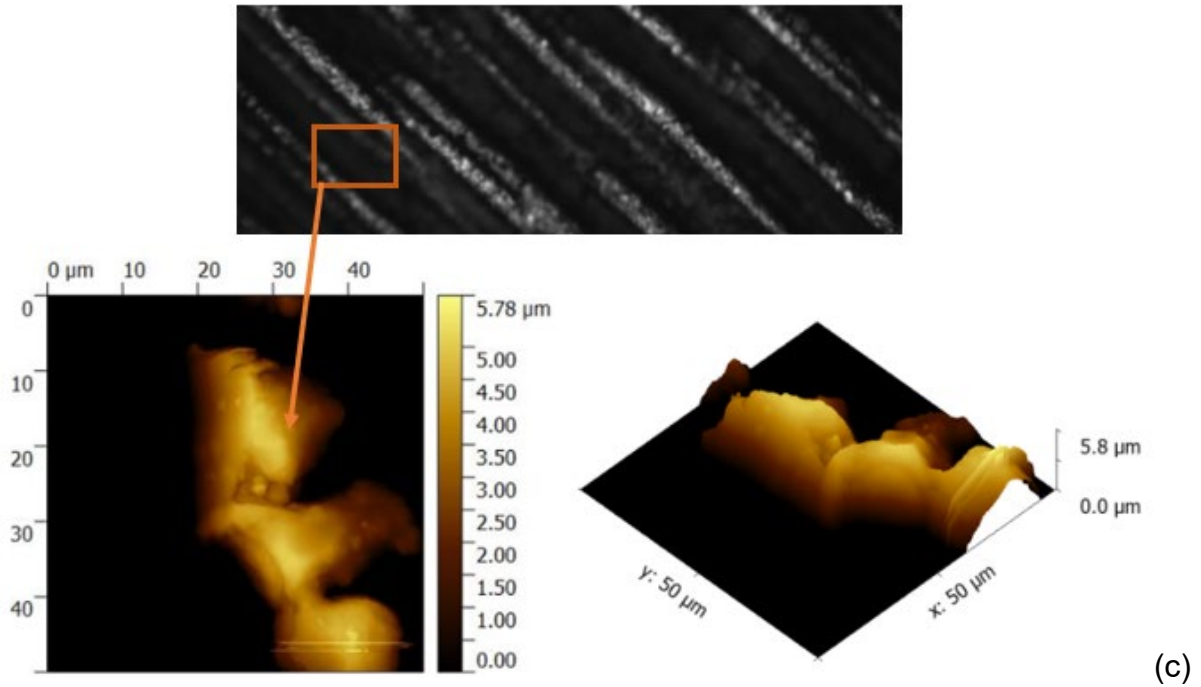

(a)

Branch N3-1 (upper branch)

θ_3

Network 3

Branch N3-2 (lower branch)

θ_1

Network 1

θ_2

Network 2

θ_4

Network 4 (b)

(c)

Fig. 1 Schematics of (a) the experimental setup; (b) structure of Networks 1-4 with the branch angle varying from 12˚ to 66˚ from the horizontal view; (c) brightfield microscope image of the regular patterns on the laser-treated surface, and the tapping mode AFM images on the ridge of the pattern line for the scan area 50 × 50 μm.

Table 1. Physical properties of DI water and aqueous solutions of glycerol (at 25°C and atmospheric pressure[36])

Glycerol wt %	Viscosity (×10⁻³ Pa·s)	Surface tension (mN/m)	Density (kg/m³)
Glycerol 100	220	66.5	1235
Glycerol 60	11.7	68.5	1156
Glycerol 40	3.64	70.0	1100
0 (DI water)	1.002	72.0	998

Flow visualization and quantification of bubble velocity

During the bubble removal, the entire bubble was visualized and tracked in a sequence of images by the high-speed camera (Chronos 1.4) fitted with a 4.5 x objective lens (Edmund Industrial Optics). The frame rate and exposure time were adjusted to capture clear images for individual bubble removal experiment. The bubble velocity was defined as $u_b = \Delta D_b / \Delta t$, in which ΔD_b corresponding to the distance that the bubble travels over the time Δt. The axial position of the bubble was identified and both ΔD_b and Δt can be quantified through processing the recorded images, as shown in Fig. 2.
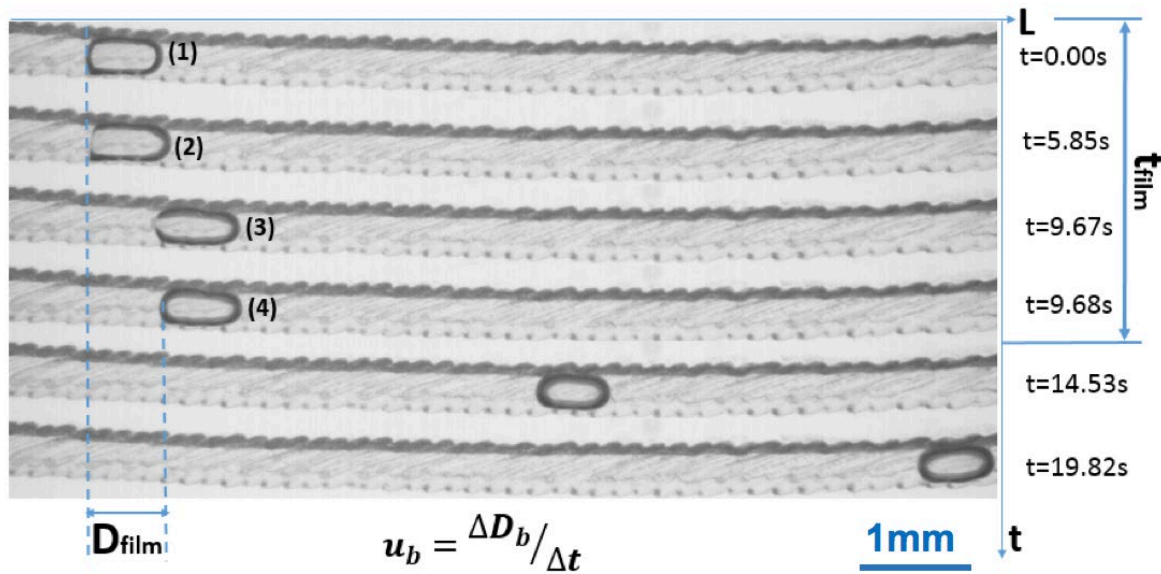
Fig. 2 Method for quantitative visualization of the dynamics of a bubble with the initial length of 0.7mm during the bubble removal from Branch N1-2, and the working liquid is glycerol 60 wt. %. Sample snapshots were obtained when the bubble travels from the left to right of the focused region, and the sequences of bubble images were recorded at 1057fps. D_{film} is the bubble moving distance required for depositing a complete and continuous liquid film around the bubble. The deposition of complete

liquid film is achieved when tiny droplets and dry patches in the area disappear, and the corresponding time is defined as t_{film} which is the time required for the formation of a continuous and steady thin liquid film between an initially dry, lodged bubble and channel wall.

Capillary number ($Ca = \mu u_b / \sigma$), which characterizes the relative effect of viscose force versus surface tension acting across an interface between a liquid and a gas phase, is based on the bubble velocity u, liquid viscosity μ and surface tension σ. Reynolds number ($Re = \rho u_b r / \mu$, where r is the radius of the microchannel) characterizes the relative magnitudes of inertial and viscous effect. Bond number ($Bo = \rho g r^2 / \sigma$, where g is the gravitational acceleration), measures the relative importance of gravitational force over surface tension force. In the study, for glycerol 60 wt. % $Bo \approx 2.2 \times 10^{-2} \ll 1, Ca \leq 1.4 \times 10^{-4}, Re \leq 4.7 \times 10^{-2}$ and for DI water $Bo \approx 2.6 \times 10^{-2} \ll 1, Ca \leq 2.1 \times 10^{-4}, Re \leq 4$. The gravitational force can be ignored ($Bo \ll 1$)[37], and the effect of surface tension has been taken into account in this study as Ca is lower than 10^{-4}.

Results and discussions

Evolution of liquid film surrounding a dry bubble

High-speed visualization of the bubble removal process reveals the evolution of the liquid film deposition between the lodged, dry bubble and channel wall. For a dry bubble which is pinned on the surface of the channel, i.e. case (1) in Fig. 3, the driving pressure is not sufficient to overcome the pinning force of the lodged bubble and the

bubble remains lodged. With slowly increasing the liquid flowrate of the driving pump, the bubble starts to deform and then move once the driving pressure gradually reaches the threshold. The liquid in the corner is pushed into the central region of contact area between the bubble and channel wall. The contact line becomes non-continuous, and a parabolic shape of a liquid film is gradually formed with the maximum film thickness located at the central wall, as shown in cross-sectional plane of the microchannel (Fig. 3). Khodaparast et al.[13] and Kreutzer et.al.[14] both demonstrated that dewetting of a liquid film on low-wettability surfaces starts from the point with the smallest film thickness, which is in the vicinity of the valleys as shown from the cross-sectional view in Fig. 3. The liquid rupture starts from the valley regions during the dewetting process. In reverse, the formation of liquid film starts from the same region during wetting process. At the early stage of bubble removal, the deposition of liquid film is metastable. The thickness of the liquid film formed between the moving bubble and channel wall is so thin that the liquid film may immediately rupture, as shown in Figs. 3 (2) and 3 (3). With the progression of bubble movement, the film thickness (h) increases with the increase of bubble velocity as the scale of $u_b^{2/3}$ according to the lubrication theory[17]. The rupture time of liquid film scales with $h^{5/7}$, thus the rupture time (or lifetime) of liquid film increases progressively[14]. The fully wetted regime is achieved as the bubble velocity is greater than the film dewetting velocity (i.e. the speed of the moving contact line of the three phases) and the lifetime of the liquid film is longer than the convective time of the bubble. Continuous and steady liquid film is fully deposited and surrounding the bubble, and it is the moment when the bubble converts from the dry to lubricated state. At the lubricated state, the thin liquid film facilitates the bubble movement with less energy dissipation as the pinning of the contact line on the surface disappears.
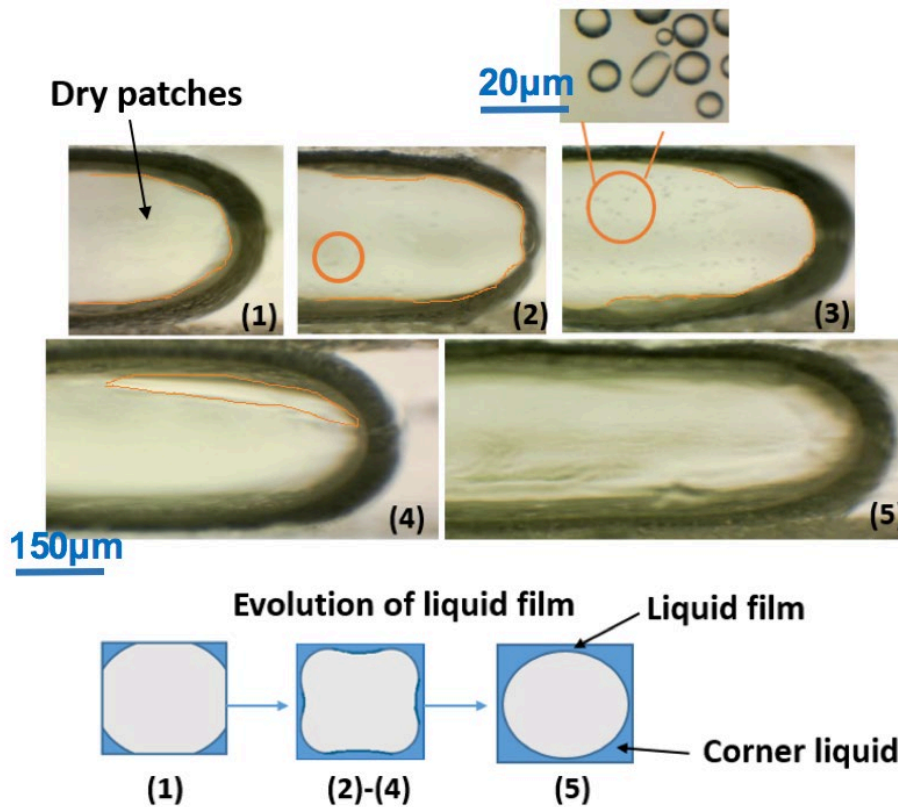
Fig. 3. Schematics of the snapshots by the high-speed visualization during a dry bubble removal process from the Branch N1-2, and the working liquid is DI water. (1) Dry (non-wetting) bubble at the static state, t=0.00s; dry patches are clearly shown and indicated as the orange contours; (2)-(5) the evolution of liquid film deposition with the dynamics of bubble; the liquid droplets which are highlighted by the orange circles are formed due to the rupture of the metastable liquid film. The two-dimensional liquid and gas distribution from the view of the cross-section has been presented. Light grey region is the gas phase and blue region is the liquid phase, and the thickness of the liquid film is exaggerated for illustrative purposes.

Relationship between bubble velocity and the liquid film deposition

The total pressure drop is composed of the pressure drop in corner liquid, capillary pressure drop, frictional pressure drop and pressure drop caused by liquid film deposition, i.e. $\Delta P_{total} = \Delta P_{corner} + \Delta P_c + \Delta P_{film} + \Delta P_{fric}$.

The drag force acting on a bubble in a square microchannel is originated from the corner liquid (blue regions) , as shown in Fig. 4. The pressure difference $(P_{back} - P_{front})$ between the front and back of the bubble should be equal to the pressure drop for the corner liquid. As the corner liquid can be approximately regarded as the Poiseuille flow[22, 38], Hagen-Poiseuille equation is given to calculate the pressure drop for corner flow as,

$$P_{back} - P_{front} = \frac{8\mu l_b Q_{corner}}{\pi r_{corner}^4} = \frac{8\mu l_b u_{corner}}{r_{corner}^2} \tag{1}$$

$$F_{corner} = \int_{A_0}^{A} \int_{x_0}^{x_m} \frac{dp}{dx} \, dx dA = C_{corner} A_b \frac{8\mu l_b}{r_{corner}^2} * u_{corner} \tag{2}$$

The velocity of corner liquid can be roughly assumed as $u_{corner} \approx u_b * c'(\frac{4}{4-\pi})$, and the derivation process can be found in Supporting Information. The equation (2) becomes,

$$F_{corner} = C_{corner} A_b \frac{8\mu l_b}{r_{corner}^2} * \left(\frac{4}{4-\pi}\right) * u_b \tag{3}$$
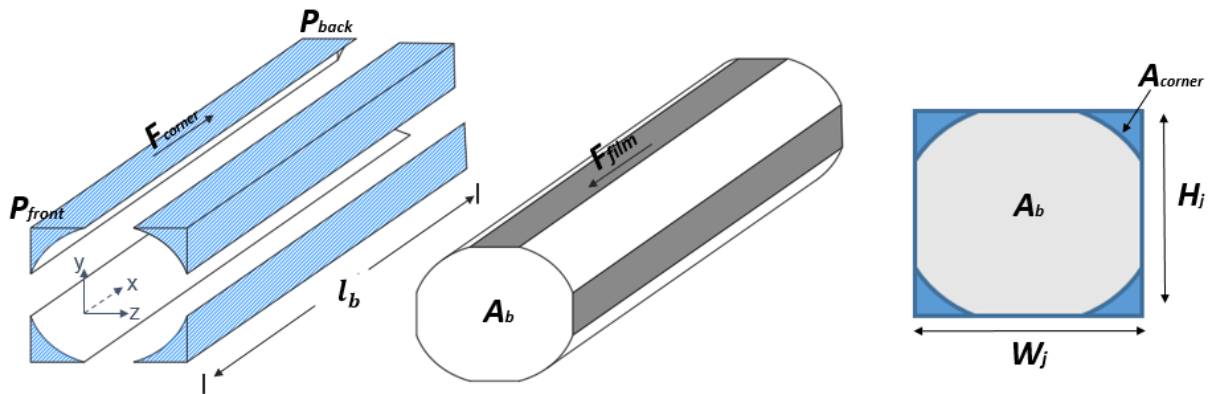
Fig. 4 Schematics of a bubble of length l_b in a square microchannel which is filled with liquid. A_b is the cross-sectional area of the bubble; A_{corner} is the cross-sectional area of the corner flow. W_j and H_j is the width and height of microchannel j in which the bubble resides. A coordinate system is fixed at the nose of the bubble with x pointing downstream.

The capillary pressure drop for rectangular microchannels is given by the derived Young-Laplace equation, as[32],

$$\Delta P_c = \frac{2\sigma}{r}(\cos\theta_{rec} - \cos\theta_{adv}) \tag{4}$$

$$r \approx \frac{W_j * H_j}{W_j + H_j}$$

Where r is the equivalent radius of the microchannel. The dynamic (advancing or receding) contact angle (θ_d) is the function of the static contact angle (θ_s) and interface velocity (u_b), and it can be expressed as[39-40],

$$\cos\theta_d = \cos\theta_s \pm 2(1 + \cos\theta_s)\sqrt{\frac{\mu u_b}{\sigma}} \tag{5}$$

The variation in dynamic contact angle induces a curvature difference between the front and back of the bubble. The capillary force can be calculated through integration of the capillary pressure over the surface area,

$$F_{cap} = C_{cap} A_b \sigma \frac{1}{r}(\cos\theta_{rec} - \cos\theta_{adv}) \tag{6}$$

$$A_b \approx \pi R * r \tag{7}$$

Where R is the radius of the curvature.

The pressure drop (ΔP_{film}) required for depositing a thin liquid film between a bubble and channel wall has been investigated by Bretherton[17] and Wong[41], and the expression has been established in the range $10^{-5} < Ca < 10^{-2}$, given as,

$$\Delta P_{film} = \frac{C_D \sigma}{r} * Ca^{2/3}$$

Where C_D is the coefficient, depending on the geometry of the cross-section of the microchannel, and the values for various polygonal microchannels can be found in Wong[41]. This equation is valid in this study ($Ca < 2.1 \times 10^{-4}$). The induced force (F_{film}) pushes the liquid into the region between the dry bubble and the channel wall, and it gives,

$$F_{film} = \frac{C_D A_b \sigma}{r} * Ca^{\frac{2}{3}} = \left(\frac{C_D A_b \sigma^{\frac{1}{3}} \mu^{\frac{2}{3}}}{r} \right) * u_b^{\frac{2}{3}} \tag{8}$$

The frictional force (F_f) arises from the channel wall when the bubble interface directly contacts with the channel surface. The friction force highly depends on the surface roughness, and it is normally neglected due to the use of smooth surface in previous investigations. However, as the PMMA surface is harshly etched by the laser, and the AFM measurement indicates that the surface is rough, the friction is considered in this study. It can be assumed as the function of the length of contact line (D_c) between bubble phase and channel surface, and the surface tension[29].

$$F_f = C_f \sigma D_c \tag{9}$$

Where C_f depends on the surface properties. The surface properties of microchannel in the study have been controlled to be identical to ensure a very similar C_f value for Networks 1-4.
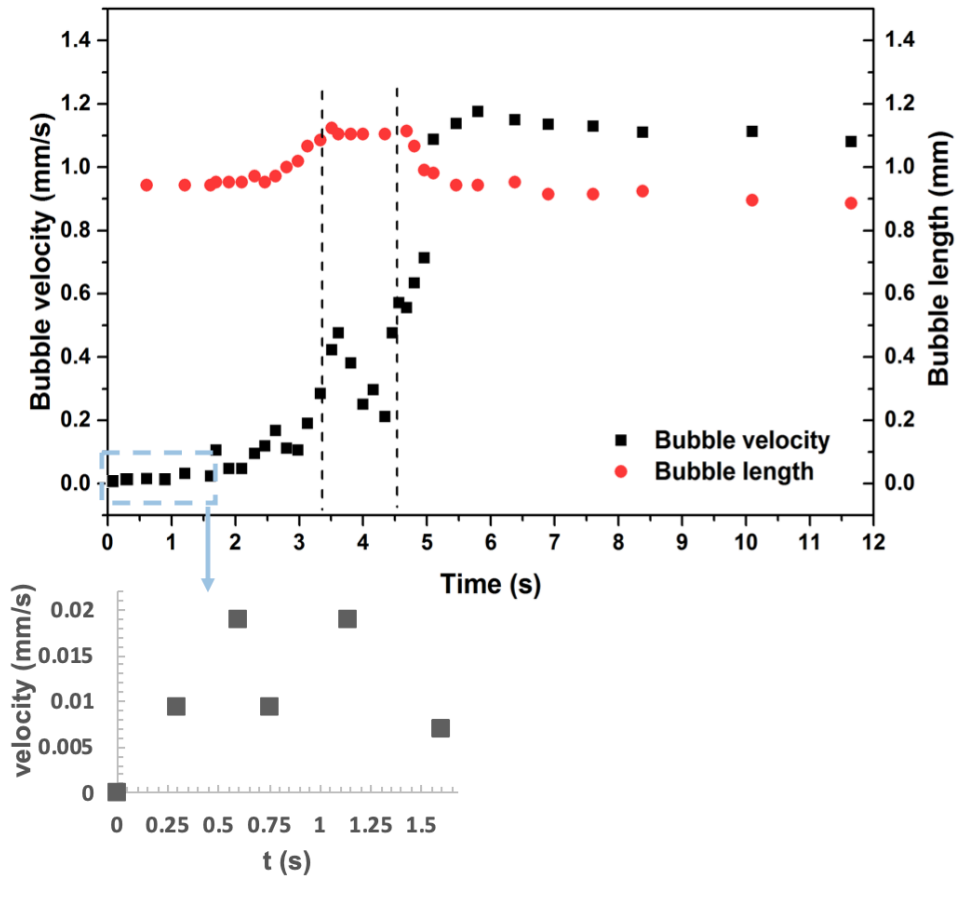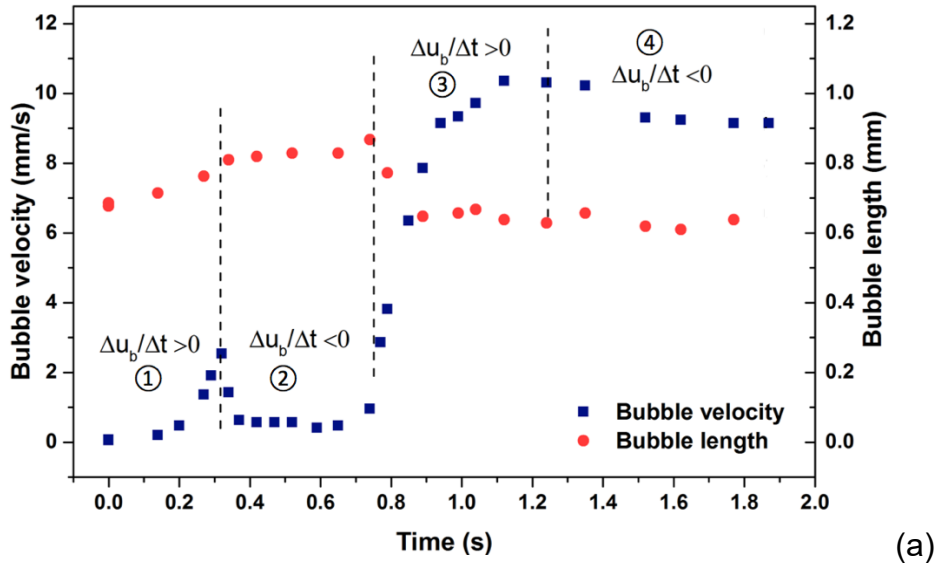
Fig. 5 Bubble velocity profiles and the variation of bubble length during a bubble removal process from Branch N3-2 with (a) DI water and (b) glycerol 60 wt. % solution

as the working liquid. The time ranges from the point when the bubble is initiated to move to the time when the bubble moves out of the field of view.

The bubble velocity profiles, i.e. variation of bubble velocity with time during the bubble removal have been plotted in Figs. 5(a) and 5(b). Generally, the bubble velocity in DI water is an order faster than in glycerol 60 wt. %. The reasonable explanation is that the bubble suffers a much higher viscous force (11 times) in glycerol 60 wt. % solution, which may hinder the increase in bubble velocity. The bubble velocity profile reveals the initiation of bubble removal, the evolution of liquid film deposition around the dry bubble, the relationship between the evolution of liquid film with the superficial bubble velocity, and the interaction of forces during the bubble removal.

There are four stages in the bubble velocity profiles for both DI water and glycerol solutions, as shown in Figs. 5(a) and 5(b). The dry bubble was stuck initially due to contact angle hysteresis at an extremely low liquid flowrate. The liquid flows through corners which attempts to drag the bubble. Once the driving force originates from the corner liquid overcomes the contact line pinning, the bubble moves forward with a slight increasing velocity at the stage ① $\frac{\Delta u_b}{\Delta t} > 0$, $F_{corner} - F_{cap} - F_f - F_{film} > 0$. The frictional force ($F_f$) is induced subsequently as another resistance when the bubble starts to move due to the movement of the contact line between the dry bubble and the rough channel wall. At the beginning of the stage ① (as shown in the inserted figure of Fig. 5b), the fluctuation of bubble velocity at the very low velocity was observed, which can be explained by bubble 'stick-slip' behaviour[42-43]. The contact line of the bubble is firstly pinned on the rough surface, and the contact angle of bubble interface is decreased to against the increase of the driving force. When the contact

angle is equal to the receding contact angle of the bubble interface, the bubble contact line moves forward. After the slip, the bubble contact angle returns to its original value and the contact angle becomes pinned again. The slip-stick behaviour lasts shortly as the driving pressure is gradually increasing.

After the initiation of bubble movement, the dynamic contact angle changes with the bubble velocity, which attributes to the difference in curvature between the front and back of the bubble, i.e. the capillary pressure drop. With the increase of the bubble velocity, the liquid film is gradually deposited between the bubble and channel wall. In addition, frictional force (F_f) increases with the contact line between the bubble and channel surface due to the bubble elongation. The relative contribution of each force has been predicted through Equations (3)-(9). As shown in Fig. 6, even though the driving force increases with the increase in the corner liquid velocity, the increase in the resistant force (F_{film}) and frictional force (F_f) leads to: $F_{corner} - F_{cap} - F_f - F_{film} < 0$, i.e. stage ②.
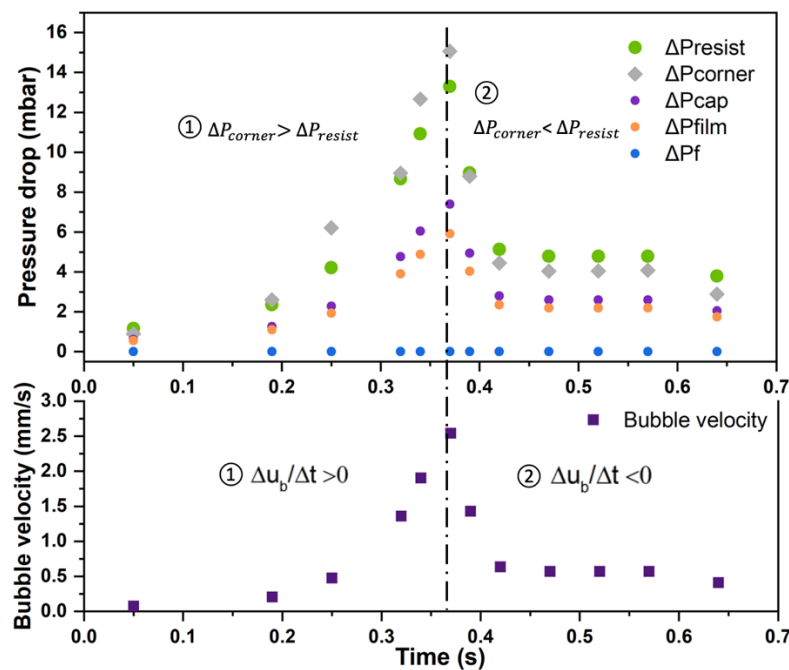
Fig. 6 Bubble velocity profile and pressure drop profiles during the stages ① and ② of the bubble removal process from Branch N3-2 with DI water, in which ΔP_{resist} is the overall pressure drop caused by the capillary force, friction force and liquid film deposition.

At the stage ③, $\frac{\Delta u_b}{\Delta t} > 0$, $F_{corner} - F_{film} > 0$. With the increase of bubble velocity, the liquid film fully deposits between the moving bubble and channel surface, which leads to the fact that the three-phase contact line among the channel surface, bubble and liquid vanishes. In this case, both the capillary force and friction force, which acted as the main resistance at the stages ① and ②, becomes negligible. The driving force is much greater than the resistant force, therefore, the velocity of the bubble increases at a significant rate. The maximum bubble velocity should be less than the corner liquid velocity at this stage.

At the stage ④ as shown in Fig. 5, $\frac{\Delta u_b}{\Delta t} < 0$. Bubble velocity profiles show a slight decrease in the velocity within the limited region of interest (field of view). More bubble velocity profiles have been provided as Supporting information to further demonstrate this slight decrease in bubble velocity in both DI water and glycerol solutions. To move a lodged bubble in a micro channel, the pressure applied to the bubble is slightly higher than the pressure required to maintain the bubble moving at the constant velocity in the channel. The slight high pressure is to overcome the inertia of the lodged bubble. Once the bubble is accelerated to the highest velocity, the pressure applied to the bubble slightly decrease to match the pressure provided by the pump to maintain the fluid motion. The bubble velocity will slightly reduce as shown in the phase 4, and then

reach the terminal velocity, which is out of the field view of this microscope. ~~With the progression of bubble movement, no driving force is available once the bubble velocity reaches its maximum as the liquid velocity is slightly lower than the maximum bubble velocity based on the previous research presented by Fairbrother and Stubbs[45]. Even for very tiny bubbles ($l_b \to 0$), the bubble velocity is nearly the same with the liquid velocity (Thome et al.)[46]. In this case, the bubble only suffers from the resistant force without corner liquid driving force, leading to a slight decrease in bubble velocity.~~ In addition, the inhomogeneous surfactant distribution on the bubble-liquid interface results in the surface tension gradients (i.e. Marangoni stress) which tends to immobilize the bubble interface[47]. Eventually, the bubble velocity will reach a constant when the resistant force is balanced by the fluid driving force before the bubble moves out of the channel.

The maximal bubble velocity (u_{bmax}) should achieve the condition:

$$F_{corner} = F_{film}$$

$$C_{corner} A_b \frac{8\mu l_b}{r_{corner}^2} * \left(\frac{4}{4-\pi}\right) * u_{bmax} = \left(\frac{C_D A_b \sigma^{\frac{1}{3}} \mu^{\frac{2}{3}}}{r}\right) * u_{bmax}^{\frac{2}{3}} \quad \to \quad (u_{bmax})^{-\frac{1}{3}} = K l_b \tag{10}$$

$$K = \left(\frac{C_{corner} * 32 * r}{C_D * r_{corner}^2 * (4-\pi)}\right) * \left(\frac{\mu}{\sigma}\right)^{\frac{1}{3}} \tag{11}$$

The K is mainly dominated by the viscosity and surface tension of the liquid, as the first blanket in equation (11) can be approximately regarded as a constant for bubbles residing in the microchannel with the identical cross-sectional shape and dimension. For two different working liquids (DI water and glycerol solution), it gives,

$$\frac{K_D}{K_G} = \left.\left(\frac{\mu_D}{\sigma_D}\right)^{\frac{1}{3}} \middle/ \left(\frac{\mu_G}{\sigma_G}\right)^{\frac{1}{3}} \approx 0.44 \right. \tag{12}$$
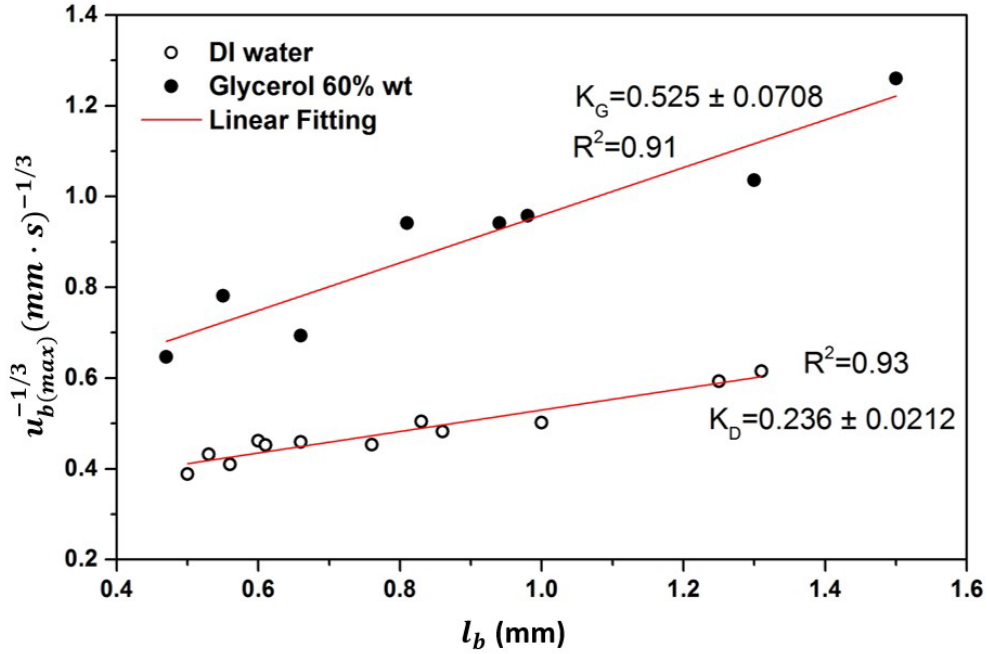

Fig. 7 Plots of $(u_{bmax})^{-\frac{1}{3}}$ and l_b for DI water and Glycerol 60 wt. % in the Branch N3-2. The values of slope K_G and K_D are obtained through linearly fitting experimental results with the equation (10).

The correlation of maximum bubble velocity (equation 10) has been derived as a function of bubble length, fluid viscosity, surface tension, geometry of cross-sectional area and dimension of microchannel, which agrees well with the experimental results. If bubbles were in the same branch with the same working liquid, the bubble with a larger length would have smaller u_{bmax}. To verify equation (10), the maximal bubble velocity experimentally obtained has been plotted with bubble length in Fig. 7. The experimental results demonstrate the correlation between $(u_{bmax})^{-\frac{1}{3}}$ and l_b for

removing bubbles of various lengths from the same branch with two different working liquids. The u_{bmax} decreases with the increase of bubble length as $(u_{bmax})^{-\frac{1}{3}} \propto K l_b$ for both DI water and Glycerol 60 wt. %. The ratio of K values $(\frac{K_D}{K_G})$ is equal to 0.449, and this value is in excellent agreement with the theoretical result of 0.44 (as shown in equation 13), with the deviation of 2%.

Effect of network angle and liquid properties on D_{film}

The bubble moving distance required for depositing a continuous and steady liquid film between the bubble and channel wall was defined as D_{film}. From Fig. 8, comparison among three different flow regimes shows that D_{film} tends to be larger in DI water, and the explanation is given in the next section. The network branch angle also affects D_{film}. The branch with a greater angle (Branch N3-2) requires a higher D_{film} to fully deposit the liquid film surrounding the bubble. In glycerol 60 wt. % solution, D_{film}/l_b is gradually approaching 1 with the increase of the bubble length. It suggests that bubbles with a greater length ($\frac{l_b}{H} > 4$) are more likely to be the lubricated state in glycerol 60 wt. % solution. This agrees well with experimental observation as bubbles with long length ($\frac{l_b}{H} > 4$) were always observed at the lubricated state in glycerol 60 wt. %, and the pressure drop for removing a longer bubble was much lower.
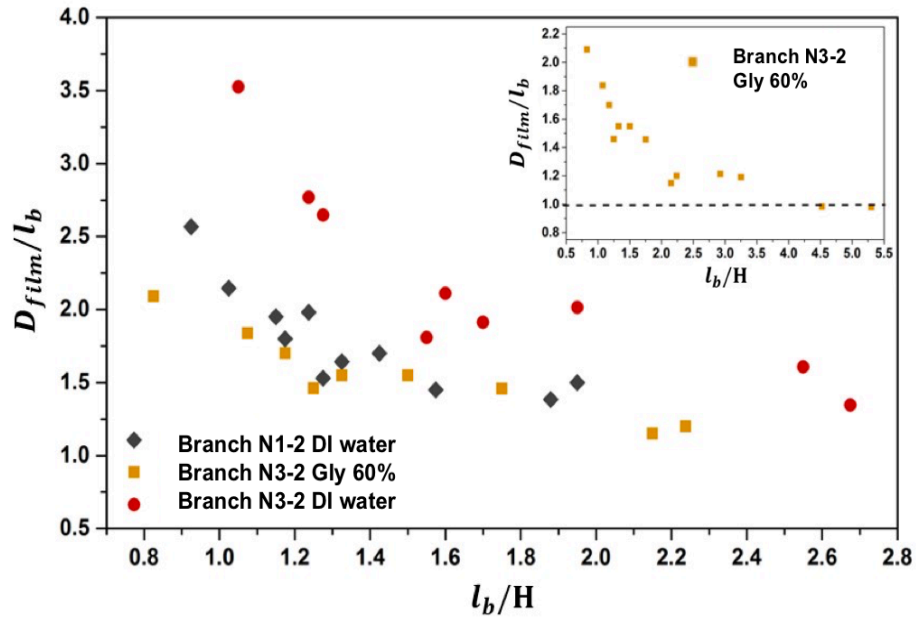
Fig. 8 Effect of network branch angle and liquid properties on the relationship between D_{film} and l_b. D_{film} and l_b are dimensioned by the parameter of bubble length (l_b) and microchannel height (H). The angle in Branch N1-2 and Branch N3-2 is 12˚ and 55˚, respectively.

Effect of liquid film on the pressure drop for bubble removal

The liquid film significantly affects the resistance to remove the lodged bubbles from the microfluidic network. Two types of bubbles, dry bubble and (partially) lubricated bubbles can be observed during the bubble removal, and typical examples are shown in Fig. 9. The pressure drop for removing a dry bubble is much higher than that for a lubricated bubble with the same length in the same flow regime. The dry bubble contacts the interior wall of the channel, and thus both frictional force and capillary force along the contact lines have to be overcome to initiate the bubble movement. For the lubricated bubble, the liquid film acts as a lubricating film, and the three phase boundary disappeared, thus the bubble does not suffer from friction force which is

originated from the movement of the three-phase boundary. Once the bubble is lubricated, capillary force from the three-phase boundary is no longer a dominant factor (Ca number > 10^{-5})[47-48],.

In Fig. 9, the plot of pressure drop and bubble length for partially lubricated bubbles is scattered. For the bubble with the same length, the pressure drop varies with the degree of lubrication which is very difficult to evaluate. The correlation between pressure drop and bubble length for the removal of a dry bubble in microfluidics filled with DI water has been derived previously, and the details can be found in references[31-32]. Our experimental results (Fig. 9) agree well with the equation (13), suggesting that equation (13) can describe well the dry bubble removal from microfluidic networks filled with different working liquids.

$$\Delta P = \frac{\pi r_{corner}^4 L_j}{16 K W_j H_j c_j} \left[\frac{\sigma(\frac{1}{W_j}+\frac{1}{H_j})(\cos\theta_{rec}-\cos\theta_{adv})}{l_b} + \frac{\rho_l f_f u_b^2}{H_j} \right] \tag{13}$$

Where K is the absolute permeability of the microchannel, L_j is the bubble moving distance, ρ_l is the density of working liquid, and f_f is the frictional factor, which is closely related to fluid velocity and viscosity. Parameter c_j is a coefficient characterizing the pressure loss due to the network structure. c_j is a constant and is independent of the fluids properties (such as gas and liquid surface tension or viscosity) and bubble length.
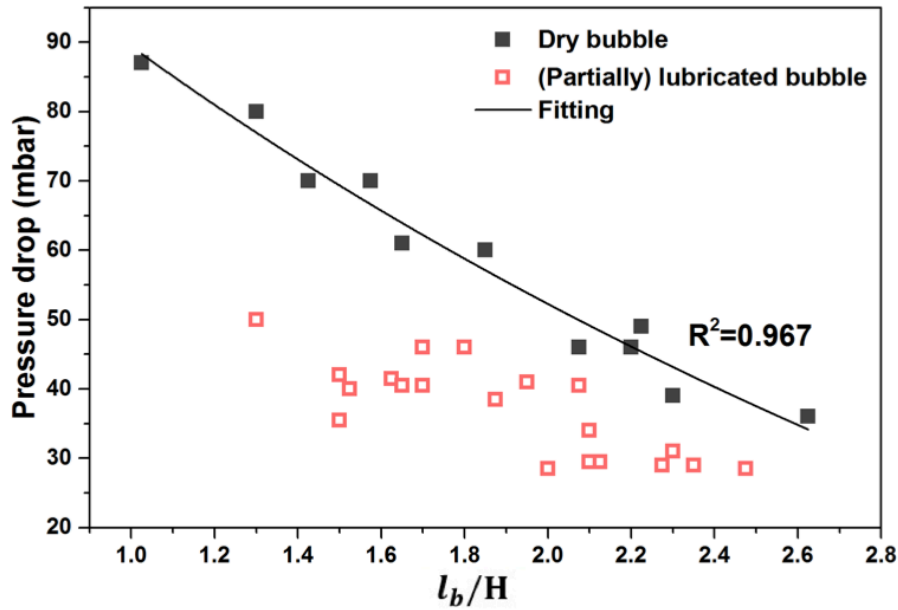
Fig. 9 Pressure drop profiles for removing dry and lubricated bubbles with various lengths from Network 1, the working liquid is glycerol 60 wt. %. We only focus on the bubble with the length for $1 \leq \frac{l_b}{H} \leq 3$, as dry bubbles with long length ($\frac{l_b}{H} > 4$) in glycerol 60 wt. % was not easily observed.

An air bubble is more likely to be lubricated in glycerol solutions than in DI water, which was demonstrated both by the relatively smaller D_{film} value before stage 3 as shown in Fig. 8, and by the fact that (partially) lubricated bubbles was frequently observed with glycerol solution during experiments. There are several explanations. As glycerol is a surfactant, when glycerol molecules adsorb on air/water interface, the carbon chains insert to air phase and the hydroxyl groups insert to water phase, therefore reducing the interfacial energy between air, liquid and solids to facilitate the spreading of liquid film between bubble and the channel wall. Glycerol can also enhance the interaction force between the liquid and solid surfaces to facilitate water spreading. H-

bonds interaction in water is weaker than in glycerol solutions, which can be proven by comparing the average numbers of hydrogen bond per water (or glycerol) molecule based on the molecular dynamics simulation[48]. The highly polar H-bond in glycerol solutions acts as a strong force to facilitate the formation of liquid film and increases the stability of liquid film. On the other hand, Ca number of the bubble-glycerol system (5×10^{-6}-7×10^{-5}) is approximately an order of larger than the Ca number of the bubble-DI water system (1.0×10^{-6}-6.6×10^{-6}). Ca number represents the relative effect of viscous versus capillary force. The deposition of thin liquid film mainly involves two contributions- capillary force which sucks fluid from the thin liquid film; and motion of corner liquid which drags the liquid into the film. This suggests that a higher Ca number promotes the deposition of the thin liquid film, which may explain why the liquid film is more easily formed between the bubble and channel wall in glycerol than in DI water system.

In addition, when glycerol wt. 40% and glycerol wt. 60% were used as the working liquid, small bubbles were observed to be perfect spheres, which agrees with the experimental results observed by Xiong, et al[49]. The relative spherical shape suggests the bubble in glycerol solution tends to minimize the surface area, which facilitates bubble movement in microfluidics devices due to the smaller surface energy.

Effect of liquid properties and branch angle on the pressure drop for dry bubble removal

The pressure drop for removing dry bubbles with different working liquids have been plotted as a function of bubble length in Figs. 10 (a) and 10 (b). It suggests that the pressure drop increases with the increase in liquid viscosity from 1.0 cP (DI water) to

11.7 cP (glycerol 60 wt. %), which agrees well with the equation (13). Comparing Fig 10(a) with Fig. 10(b), it suggests that the effect of viscosity on bubble removal is hindered by the increase in the branch angle. For bubbles with larger length, the effect of both liquid viscosity and network branch angle is trivial. Taking a bubble with a length of 0.5 mm as an example, when the viscosity increases from 1 to 11.7 cP, the pressure drop increases from 24 to 79 mbar in the Branch N1-2 with a branch angle of 12˚. However, the increase in pressure drop ranges only from 53 to 90 mbar in Branch N3-2 with a branch angle of 55˚.

It is worth to mention that the increase in liquid viscosity also eases the effect of branch angle on the dry bubble removal. The pressure drop increases with the increase in the branch angle, which can be explained by the equation 10. However, the difference in pressure drop for removing bubbles from Networks 1-4 with DI water (Fig. 10c) is much larger than that when glycerol 40 wt. % is used as the working liquid (Fig. 10d). For example, with the increase of the branch angle from 12˚ to 66˚, the pressure drop to remove a bubble with a length of 0.6 mm increases from 52 to 75 mbar when the working liquid is glycerol 40%wt. In the case of DI water, the difference changes widely from 20 to 70 mbar.
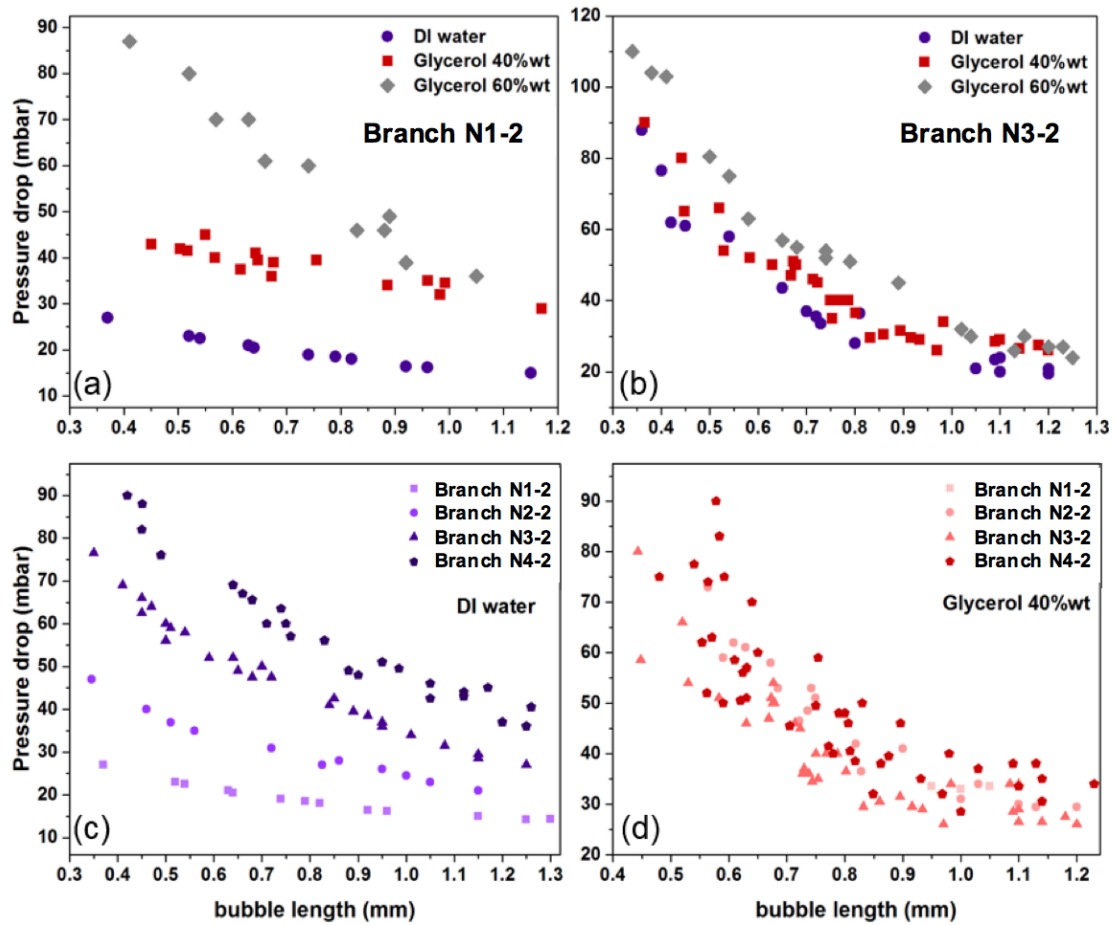
Fig. 10 Pressure drop for dry bubbles removal in working liquids with different viscosity from (a) Branch N1-2 and (b) Branch N3-2; pressure drop profiles for dry bubble removal from the Branch N1-2 to Branch N4-2 for the working liquid (c) DI water and (d) glycerol 40 wt. %. Branch angles of network the lower branch of Networks 1-4 (Branch N1-2 to Branch N4-2) are 12˚, 25˚, 55˚ and 66˚, respectively.

Conclusions

Experiments and modelling were performed to visualize and analyze the spatiotemporal evolution of liquid film deposition between the dry bubble and rough surface wall in microfluidic networks. The results show that the initial movement of the

dry and lodged bubble from a microchannel experiences four different stages. 1) Dry bubble was first driven to move at a slight increased bubble velocity to a very short distance. 2) The liquid film starts to deposit between the dry bubble and the rough surface wall, and the deposition process resists bubble movement, resulting in the decrease of the bubble velocity. 3) Once the liquid film is fully deposited surrounding the bubble, the bubble velocity start to significantly increases as both the friction force and capillary force are negligible with the vanish of three-phase contact line. (4) Plug flow dominates the bubble movement and the bubble fully converts from dry state to lubricated state, which moves at the energy-saving mode.

The deposition of the liquid film surrounding the bubble significantly affects bubble removal process and the superficial velocity of the bubble. The correlation of maximum bubble velocity has been derived as a function of bubble length, fluid viscosity, surface tension, geometry of cross-sectional area and dimension of microchannel, which agrees with the experimental results. The bubble moving distance and pressure drop required for a full deposition of a continuous and steady liquid film around a bubble are affected by the viscosity of working liquid and network branch angle. The liquid with a high viscosity will increase the pressure drop for removing dry bubbles, and this impact is eased by increasing the network structure complexity. For partially lubricated bubbles, the deposition of liquid film significantly reduces the pressure drop for removing bubbles from the microfluidic network. Glycerol 60 wt. %, compared with DI water, is proven to act as a 'lubricating' liquid to easily remove bubbles.

Reference

1.   Günther, A.; Jensen, K. F., Multiphase microfluidics: from flow characteristics to chemical and materials synthesis. *Lab Chip* **2006,** *6* (12), 1487-1503.
2.   Schwarzkopf, J. D.; Sommerfeld, M.; Crowe, C. T.; Tsuji, Y., *Multiphase flows with droplets and particles*. CRC press: 2011.
3.   Eain, M. M.; Egan, V.; Punch, J., Film thickness measurements in liquid-liquid slug flow regimes. *Int. J. Heat Fluid FL.* **2013,** *44*, 515-523.
4.   Miller, C. T.; Christakos, G.; Imhoff, P. T.; McBride, J. F.; Pedit, J. A.; Trangenstein, J. A., Multiphase flow and transport modeling in heterogeneous porous media: challenges and approaches. *Adv. Water Resour.* **1998,** *21* (2), 77-120.
5.   Grossman, G., Simultaneous Heat and Mass-Transfer in Film Absorption under Laminar-Flow. *Int. J. Heat Mass Transf.* **1983,** *26* (3), 357-371.
6.   Danckwerts, P. V., Significance of Liquid-Film Coefficients in Gas Absorption. *J. Ind. Eng. Chem.* **1951,** *43* (6), 1460-1467.
7.   Rebrov, E. V.; Berenguer-Murcia, A.; Skelton, H. E.; Johnson, B. F.; Wheatley, A. E.; Schouten, J. C., Capillary microreactors wall-coated with mesoporous titania thin film catalyst supports. *Lab Chip* **2009,** *9* (4), 503-6.
8.   Han, Y.; Shikazono, N., Measurement of the liquid film thickness in micro tube slug flow. *Int. J. Heat Fluid FL.* **2009,** *30* (5), 842-853.
9.   Hazuku, T.; Fukamachi, N.; Takamasa, T.; Hibiki, T.; Ishii, M., Measurement of liquid film in microchannels using a laser focus displacement meter. *Experiments in Fluids* **2005,** *38* (6), 780-788.
10.   Aussillous, P.; Quere, D., Quick deposition of a fluid on the wall of a tube. *Phys. Fluids* **2000,** *12* (10), 2367-2371.
11.   Vrij, A.; Overbeek, J. T., Rupture of Thin Liquid Films Due to Spontaneous Fluctuations in Thickness. *J. Am. Chem. Soc.* **1968,** *90* (12), 3074-+.
12.   Yerushalmi-Rozen, R.; Kerle, T.; Klein, J., Alternative dewetting pathways of thin liquid films. *Science* **1999,** *285* (5431), 1254-6.
13.   Khodaparast, S.; Atasi, O.; Deblais, A.; Scheid, B.; Stone, H. A., Dewetting of Thin Liquid Films Surrounding Air Bubbles in Microchannels. *Langmuir* **2018,** *34* (4), 1363-1370.
14.   Kreutzer, M. T.; Shah, M. S.; Parthiban, P.; Khan, S. A., Evolution of nonconformal Landau-Levich-Bretherton films of partially wetting liquids. *Physical Review Fluids* **2018,** *3* (1), 014203.
15.   Roman, S.; Abu-Al-Saud, M. O.; Tokunaga, T.; Wan, J.; Kovscek, A. R.; Tchelepi, H. A., Measurements and simulation of liquid films during drainage displacements and snap-off in constricted capillary tubes. *J. Colloid Interface Sci.* **2017,** *507*, 279-289.
16.   Taylor, G. I., Deposition of a Viscous Fluid on the Wall of a Tube. *J. Fluid Mech.* **1961,** *10* (2), 161-165.

17.   Bretherton, F. P., The Motion of Long Bubbles in Tubes. *J. Fluid Mech.* **1961,** *10* (2), 166-188.

18.   Schubring, D.; Ashwood, A. C.; Shedd, T. A.; Hurlburt, E. T., Planar laser-induced fluorescence (PLIF) measurements of liquid film thickness in annular flow. Part I: Methods and data. *Int. J. Multiph. Flow* **2010,** *36* (10), 815-824.

19.   Kreutzer, M. T.; Kapteijn, F.; Moulijn, J. A.; Kleijn, C. R.; Heiszwolf, J. J., Inertial and interfacial effects on pressure drop of Taylor flow in capillaries. *AICHE J.* **2005,** *51* (9), 2428-2440.

20.   Stöckelhuber, K. W.; Radoev, B.; Wenger, A.; Schulze, H. J., Rupture of wetting films caused by nanobubbles. *Langmuir* **2004,** *20* (1), 164-168.

21.   Liu, Y.; Hansen, A.; Block, E.; Morrow, N. R.; Squier, J.; Oakey, J., Two-phase displacements in microchannels of triangular cross-section. *J. Colloid Interface Sci.* **2017,** *507*, 234-241.

22.   Fuerstman, M. J.; Lai, A.; Thurlow, M. E.; Shevkoplyas, S. S.; Stone, H. A.; Whitesides, G. M., The pressure drop along rectangular microchannels containing bubbles. *Lab Chip* **2007,** *7* (11), 1479-89.

23.   Zheng, W.; Wang, Z.; Zhang, W.; Jiang, X., A simple PDMS-based microfluidic channel design that removes bubbles for long-term on-chip culture of mammalian cells. *Lab Chip* **2010,** *10* (21), 2906-10.

24.   Sung, J. H.; Shuler, M. L., Prevention of air bubble formation in a microfluidic perfusion cell culture system using a microscale bubble trap. *Biomed. microdevices* **2009,** *11* (4), 731-738.

25.   Fei, K.; Hong, C. W., All-angle removal of CO 2 bubbles from the anode microchannels of a micro fuel cell by lattice-Boltzmann simulation. *Microfluid. Nanofluid.* **2007,** *3* (1), 77-88.

26.   Jose, B. M.; Cubaud, T., Formation and dynamics of partially wetting droplets in square microchannels. *Rsc Adv* **2014,** *4* (29), 14962-14970.

27.   Mohammadi, M.; Sharp, K. V., The Role of Contact Line (Pinning) Forces on Bubble Blockage in Microchannels. *J Fluids Eng* **2015,** *137* (3), 0312081-312087.

28.   Liang, M. C.; Yang, S. S.; Miao, T. J.; Yu, B. M., Minimum applied pressure for a drop through an abruptly constricted capillary. *Microfluid. Nanofluid.* **2015,** *19* (1), 1-8.

29.   Metz, T.; Paust, N.; Zengerle, R.; Koltay, P., Capillary driven movement of gas bubbles in tapered structures. *Microfluid. Nanofluid.* **2010,** *9* (2-3), 341-355.

30.   Calderon, A. J.; Eshpuniyani, B.; Fowlkes, J. B.; Bull, J. L., A boundary element model of the transport of a semi-infinite bubble through a microvessel bifurcation. *Phys. Fluids* **2010,** *22* (6), 61902.

31.   Chao, C.; X. Q. Jin; X. F. Fan, Effect of network structure on the bubble dislodgment and pressure distribution in microfluidic networks with multiple bifurcations. *Chem. Eng. Sci.* **2019**, 115176.

32.   Chao, C.; Jin, X. Q.; Teng, L. J.; Stokes, A. A.; Fan, X. F., Bubble dislodgment in a capillary network with microscopic multi-channel and multi-bifurcation features. *Langmuir* **2019**.

33.   Yousif, M. Y.; Holdsworth, D. W.; Poepping, T. L., A blood-mimicking fluid for particle image velocimetry with silicone vascular models. *Experiments in Fluids* **2011,** *50* (3), 769-774.

34.   Lim, W. L.; Chew, Y. T.; Chew, T. C.; Low, H. T., Pulsatile flow studies of a porcine bioprosthetic aortic valve in vitro: PIV measurements and shear-induced blood damage. *Journal of Biomechanics* **2001,** *34* (11), 1417-1427.

35.   Raine‐Fenning, N.; Nordin, N.; Ramnarine, K.; Campbell, B.; Clewes, J.; Perkins, A.; Johnson, I. J. U. i. O.; Obstetrics, G. T. O. J. o. t. I. S. o. U. i.; Gynecology, Determining the relationship between three‐dimensional power Doppler data and true blood flow characteristics: an in‐vitro flow phantom experiment. **2008,** *32* (4), 540-550.

36.   Takamura, K.; Fischer, H.; Morrow, N. R., Physical properties of aqueous glycerol solutions. *J. Pet. Sci. Eng.* **2012,** *98-99*, 50-60.

37.   Atasi, O.; Khodaparast, S.; Scheid, B.; Stone, H. A., Effect of buoyancy on the motion of long bubbles in horizontal tubes. *Physical Review Fluids* **2017,** *2* (9), 094304.

38.   Wong, C. W.; Zhao, T. S.; Ye, Q.; Liu, J. G., Transient capillary blocking in the flow field of a micro-DMFC and its effect on cell performance. *J. Electrochem. Soc.* **2005,** *152* (8), A1600-A1605.

39.   Li, X. X.; Fan, X. F.; Askounis, A.; Wu, K. J.; Sefiane, K.; Koutsos, V., An experimental study on dynamic pore wettability. *Chem. Eng. Sci.* **2013,** *104*, 988-997.

40.   Popescu, M. N.; Ralston, J.; Sedev, R., Capillary rise with velocity-dependent dynamic contact angle. *Langmuir* **2008,** *24* (21), 12710-6.

41.   Wong, H.; Radke, C.; Morris, S., The motion of long bubbles in polygonal capillaries. Part 2. Drag, fluid pressure and fluid flow. *J. Fluid Mech.* **1995,** *292*, 95-110.

42.   Jo, H. J.; Park, H. S.; Kim, M. H., Single bubble dynamics on hydrophobic–hydrophilic mixed surfaces. *J International Journal of Heat and Mass Transfer* **2016,** *93*, 554-565.

43.   Hatipogullari, M.; Wylock, C.; Pradas, M.; Kalliadasis, S.; Colinet, P., Contact angle hysteresis in a microchannel: Statics. *Physical Review Fluids* **2019,** *4* (4), 044008.

44.   Wong, H.; Radke, C. J.; Morris, S., The motion of long bubbles in polygonal capillaries. Part 1. Thin films. *J Journal of Fluid Mechanics* **1995,** *292*, 71-94.

45.   Fairbrother, F.; Stubbs, A. E., 119. Studies in electro-endosmosis. Part VI. The "bubble-tube" method of measurement. *J. Chem. Soc.* **1935,** *0* (0), 527-529.

46.   Agostini, B.; Revellin, R.; Thome, J. R., Elongated bubbles in microchannels. Part I: Experimental study and modeling of elongated bubble velocity. *Int. J. Multiph. Flow* **2008,** *34* (6), 590-601.

47.   Atasi, O.; Haut, B.; Pedrono, A.; Scheid, B.; Legendre, D., Influence of Soluble Surfactants and Deformation on the Dynamics of Centered Bubbles in Cylindrical Microchannels. *Langmuir* **2018,** *34* (34), 10048-10062.

48.   Chen, C.; Li, W. Z.; Song, Y. C.; Yang, J., Hydrogen bonding analysis of glycerol aqueous solutions: A molecular dynamics simulation study. *J. Mol. Liq.* **2009,** *146* (1-2), 23-28.

49.   Xiong, R. Q.; Bai, M.; Chung, J. N., Formation of bubbles in a simple co-flowing micro-channel. *J. Micromech. Microeng.* **2007,** *17* (5), 1002-1011.